

Study of clay degradation in an earthslide combining OBIA and roughness analysis of UAV-based optical images

Sylvain Fiolleau^{1,2}  | Denis Jongmans¹ | Grégory Bièvre¹ | Guillaume Chambon³ | Olivier Michel⁴ | Laurent Borgniet⁵ 

¹Grenoble Alpes University, Savoie Mont Blanc University, CNRS, IRD, Gustave Eiffel University, ISTerre, Grenoble, France

²Lawrence Berkeley National Laboratory, Earth and Environmental Sciences Area, Berkeley, CA, USA

³Grenoble Alpes University, INRAE, UR ETNA, Grenoble, France

⁴Grenoble Alpes University, CNRS, GIPSA-LAB UMR 5216, Grenoble, France

⁵Grenoble Alpes University, INRAE, UR LESSEM, Grenoble, France

Correspondence

Sylvain Fiolleau, Grenoble Alpes University, Savoie Mont Blanc University, CNRS, IRD, Gustave Eiffel University, ISTerre, 38000, Grenoble, France.
Email: sfiolleau@lbl.gov

Funding information

French national C2ROP project; French National Research Agency / Investissements d'Avenir program, Grant/Award Number: ANR-15-IDEX-02 / CDPRIK; French VOR federative structure; LabEx OSUG@2020, Grant/Award Number: ANR10 LABX56

Abstract

Flow-like landslides in clay slopes pose major threats to people and infrastructure, which has led to numerous studies in recent decades. However, the mechanisms leading to the solid–fluid transition in clay are still poorly understood, despite numerous studies on its rheological evolution. The aim of this study is to contribute to quantify the degradation of clay at the surface of the Harmalière landslide (French Alps) from the analysis of a series of three unmanned aerial vehicle (UAV) acquisitions. Two approaches were combined to process the acquired optical images. First, image classification was performed applying object-based image analysis (OBIA) to the red, green and blue (RGB) and surface roughness layers. Second, deeper analysis of the surface roughness allows to describe the morphology evolution and to interpret the degradation scheme from undegraded clay to degraded clay.

The study shows that the applied methodology is appropriate to perform a thorough analysis of the material degradation pattern on the surface of a landslide. The temporal analysis shows an average degradation rate leading to the complete degradation of a block in about 2 years. Meanwhile, a spatial analysis shows that non-degraded clays degrade faster in the lower part of the study area, reactivated 30 years ago, than in the upper part, reactivated only a few years ago. In addition, roughness analyses enabled to highlight the evolution of the morphology during the degradation process of the clay blocks, from angular blocks to mounds.

KEYWORDS

clay, degradation, earthslide, OBIA, UAV

1 | INTRODUCTION

Flow-like landslides on clay slopes are worldwide spread and pose a major menace to people and infrastructures, which has prompted numerous studies over the last 20 years (Bertello et al., 2018; Chambers et al., 2011; Fiolleau et al., 2021; Giordan et al., 2013; Mackey & Roering, 2011; Malet et al., 2005; Picarelli et al., 2005). Many of these landslides exhibit a sliding mechanism involving rigid blocks in their upper part, evolving towards a flow-like mechanism (earthflow or mudflow) at the toe. This transition implies a strong hydro-mechanical degradation of clay-rich formations (from rock or stiff soils to soft soils) due to landslide-induced deformation and surface weathering. This strong decrease in material along landslides has been quantitatively demonstrated in the clayey Avignonet earthslide

(French Alps) where the shear wave velocity (V_s) at a given depth decays by a factor of at least two from the headscarp to the toe, and is inversely correlated to the displacement rate (Jongmans et al., 2009; Renalier et al., 2010). However, a few metres thick low-velocity layer ($V_s < 200\text{--}300$ m/s) is systematically detected at the surface of clayey landslides (Bertello et al., 2018; Fiolleau et al., 2021; Renalier et al., 2010; Travelletti et al., 2013; Uhlemann et al., 2016), which can be the result of a shallow slip surface but also of weathering due to environmental factors (rainfall, drought, freezing, thawing). The degradation of the mechanical properties with weathering, through wetting–drying and freeze–thaw cycles, has been extensively studied in the laboratory on clay rock samples (Graham & Shields, 1985; Meisina, 2004; Pardini et al., 1996; Pineda et al., 2014; Zou et al., 2020). Wetting–drying cycles were shown to induce an

accumulative irreversible swelling and increase in porosity, as well as an irreversible reduction of rock stiffness and strength, associated with fissuring (e.g., Pardini et al., 1996; Pineda et al., 2014). Field observations on weathered shales in the Apennines (northern Italy) in a landslide-prone area revealed that climate fluctuations (wet-dry periods) generate swelling and shrinking cycles, which contribute to the rapid degradation of the clay material (Meisina, 2004). Shrinkage generates cracks up to metric depth in the dry season, allowing water to infiltrate into the soil and promoting weathering and sliding. Freezing has also been early identified as a major factor contributing to the development of fissures in clays (Graham & Shields, 1985; Zou et al., 2020). Comparing the effects of wetting-drying and freeze-thaw cycles, Pardini et al. (1996) found that the latter were the most effective in the structural modification of a clay mudrock. These results were corroborated by field observations on the Vallcebre landslide (eastern Pyrenees, Spain) where Regüés et al. (1995) found that the material weatherability is predominantly controlled by strong freeze-thaw cycles at high moisture values.

The combination of landslide-induced deformation and weathering then degrades the soft surficial layer and results in significant temporal and spatial changes in the landslide surface morphology (e.g., Fiolleau et al., 2021; Travelletti et al., 2013). These changes are however difficult to quantify using conventional field techniques and their monitoring requires the acquisition of high-resolution remote sensing data. In the last two decades, airborne and satellite techniques have been increasingly used to characterize the surface morphology and monitor surface changes in landslides (Baum et al., 1998; Booth et al., 2020; Lacroix et al., 2018; Stumpf et al., 2014; Wasowski & Bovenga, 2022). Developments of high-resolution digital elevation models (DEMs) make it possible to calculate and follow various attributes of the morphology such as slope, roughness and curvature for landslide characterization and monitoring (e.g., Bonetti & Porporato, 2017; Goetz et al., 2014; Hurst et al., 2013; McKean & Roering, 2004; Nappo et al., 2021; Pawluszek et al., 2018).

Two main techniques are used to create a DEM: laser scanning (light detection and ranging, LiDAR) and stereophotogrammetry using optical imagery, which is used in this study for generating elevation models. For landslide investigation, photogrammetry was initially applied from aerial plane data (e.g., Walstra et al., 2007), then from satellite images (e.g., Deilami & Hashim, 2011) and more recently from unmanned aerial vehicles (UAVs) (e.g., Peternel et al., 2017; Rossi et al., 2018). Stereoscopic image processing allows sub-metric resolution for classical airborne acquisition whereas, for satellite optical acquisition, the resolution varies from 10 m for the Sentinel-2 constellation to 0.7 m for very high-resolution satellites such as the Pleiades constellation (Lacroix et al., 2015, 2018; Stumpf et al., 2014). A significant improvement in resolution has been achieved by acquiring data from UAVs flying typically a few metres to a few tens of metres above ground surface, and which have been increasingly used for landslide mapping and monitoring (Casagli et al., 2017; Cignetti et al., 2019; Comert et al., 2019; Lucieer et al., 2014; Ma et al., 2019; Peternel et al., 2017; Rossi et al., 2018). These UAVs can be equipped with high-resolution cameras and/or LiDAR scanners and have demonstrated their ability to provide high-resolution images and DEMs with centimetric resolution on potentially hard-to-reach areas such as landslides (Eker et al., 2017; Lucieer et al., 2014). Bridging the gap between terrestrial and satellite observations, this flexible technique

seems well suited to accurately monitoring surface and morphological changes at the landslide or drainage basin scale (Nappo et al., 2021; Niethammer et al., 2012; Samodra et al., 2020).

The acquisition of an increasing number of images and the generation of DEMs have been accompanied by the development of semi-automatic and automatic processing methods to objectively and rapidly quantify the changes observed on the landslide surface. The processing can be made on the image radiometry (Puniach et al., 2021) and/or on DEM attributes such as slope and roughness values (Berti et al., 2013; Shepard et al., 2001). Among the different processing techniques, object-based image analysis (OBIA) has emerged as a predominant tool in remote sensing (Blaschke, 2010) and has recently been successfully applied to detect and map landslide-deformed areas from satellite or UAV optical images (e.g., Comert et al., 2019; Ghorbanzadeh et al., 2022; Hölbling et al., 2017; Ma et al., 2019). This technique (Ma et al., 2017) consists of first segmenting images by grouping pixels together into vectors objects and then classifying these objects using their properties (shape, spectral properties, roughness, etc.). This approach is well suited to classify objects such as landslides, scarps or clay blocks (Chang et al., 2012). Numerous algorithms such as SVM (support vector machine) and random forest can be used to classify the objects retrieved from the segmentation steps (Heleno et al., 2016; Tehrani et al., 2021). Among them, the decision tree algorithm is a simple and understandable method to predict the value of a target from several inputs and their corresponding thresholds (Ma et al., 2017).

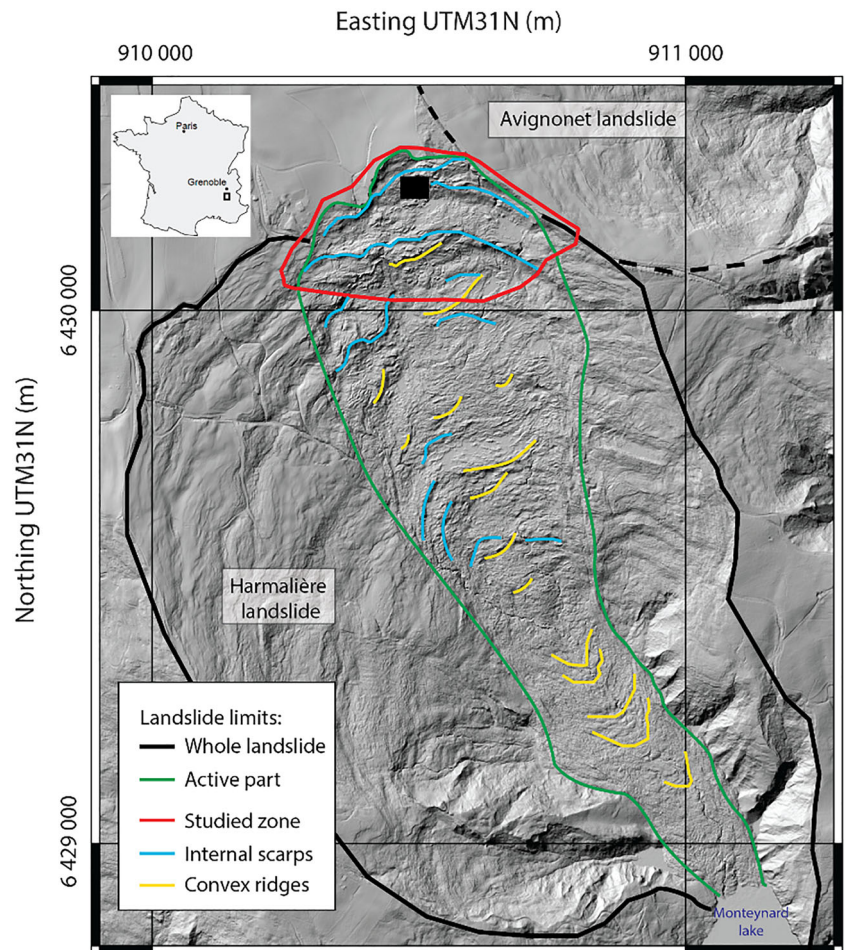
In addition, topographic spectral analysis has been already used in geomorphology to quantitatively characterize topography at different wavelengths (Berti et al., 2013; Evans, 2006). This approach has also been successfully applied to surface roughness (Chae et al., 2004).

The objective of this study is to analyse and quantify the degradation of stiff clay blocks that have slipped in the upper part of a complex landslide, using high-resolution images from three UAV acquisitions and the derived DEMs. First, we made a classification of the materials present at the surface of the landslide, using an OBIA from the radiometric properties and the roughness extracted from DEMs. We were able to identify four types of soil (intact clay, degraded clay, filling clay and surface deposits). By processing the different images, we then calculated the variations in the percentage of soil type as a function of time, which made it possible to evaluate the degradation of the clay in time and space. Second, we focused on the evolution of the roughness in time and space by performing spectral analysis, allowing a better understanding of the degradation patterns. The clay degradation was analysed at three different spatial scales: over the whole study area (about 15 ha), two intermediate sized areas (about 0.6 ha) and metric-sized blocks. As no motion was detected on the surface during the survey period, the degradation observed in this study is interpreted as resulting mainly from weathering.

2 | SITE DESCRIPTION

The Harmalière landslide is located 30 km south of the city of Grenoble, France, in the Trièves area (French Western Alps; Figure 1). Numerous landslides developing in a thick glacio-lacustrine clayey layer affect this area (Bièvre et al., 2012; Fiolleau et al., 2021; Lacroix et al., 2018). During the last Quaternary glaciation, the southward-

FIGURE 1 Location and delineation of the Harmalière landslide on a LiDAR DEM acquired on 26 November 2019. The whole landslide and the present-day active part are delimited by black and green lines, respectively. The upper part is a compound slide characterized by internal scarps (> 5 m high) with a concave shape (blue lines), while the lower part is an earthflow showing convex ridges (yellow lines). The black area delimits the zone pictured in Figure 2. [Color figure can be viewed at wileyonlinelibrary.com]



moving Romanche glacier dammed the northward-flowing Drac River, creating a lake that lasted several thousand years (Monjuvent, 1973) and was filled with a thick deposit (up to 250 m) of glaciolacustrine laminated clays. The study site is located at the tongue of the glacier and experienced successive episodes of glacier retreat and advance. This induced an alternating deposition of glaciolacustrine laminated clays and unlaminated clays mixed with pebbles originating from the moraines brought by the glacier (Bièvre & Crouzet, 2021). A layer of moraine, about 50 m thick on the plateau located a few hundred metres to the northwest and reducing to a few metres at the headscarp, caps the glaciolacustrine sequence. After the glacier melted, rivers have deeply incised the geological formations and allowed the initiation of numerous landslides.

The Harmalière landslide affects an area of around $1.8 \times 10^6 \text{ m}^2$ for an estimated volume of $45 \times 10^6 \text{ m}^3$ and a mean slope of 9° (Carrière et al., 2018; Fiolleau et al., 2021). The active zone (green line in Figure 1) is 1450 m long and 400 m wide at the top, narrowing to 150 m at the toe. The landslide has retrogressed by several hundred metres over the past 50 years (Besson, 1996; Moulin & Robert, 2004). In its upper part the landslide presents a 25 m-high headscarp, below which are found several concave internal scarps 5 to 20 m high (marked in blue in Figure 1). The mechanism at the headscarp is block sliding (Fiolleau et al., 2021). Once in the slide, the clay blocks are subject to weathering and degrade rapidly as they move downward, from sharp-edged parallelepipedal shapes to rounded shapes and to mounds of decreasing height. In contrast, the morphology of the lower part is smoother and characterized by the presence of ridges a

few metres thick with convex shapes (yellow lines in Figure 1), suggesting a flow-like mechanism. Observations suggest that these ridges are generated by multiple slip surfaces. The central part exhibits a mixture of concave and convex shapes, indicative of a transition zone between sliding and flow mechanism. On the basis of these observations, the Harmalière landslide can be categorized as a compound earthslide in its upper part and an earthflow in its lower part, according to the classification proposed by Hungr et al. (2014).

The lower part of the Harmalière landslide is covered with dense and thorny vegetation, which limits access and makes investigation in this area difficult. For this reason, the study of clay degradation based on photogrammetric data was not possible in the lower part of the landslide and was carried out only in the upper part with low vegetation density. The area covered by the UAV flights is located in Figure 1 by a red polygon. Eight classes were defined corresponding to vegetation (low and high), water, shade and four different types of soil. The different soils are presented in Figure 2 (location of the picture in Figure 1, black rectangle). The intact grey clay (orange rectangle) appears as sharp-edged slipped blocks corresponding to intact blocks composed of the succession of laminated clay and non-laminated clay with pebbles. The degraded clay (yellow rectangle) is dark grey in colour and is mixed with lighter coloured pebbles of centimetre to multi-centimetre size. The filling clay (green rectangle) results from the erosion and deposition of the degraded clay in small depressions. These clay deposits with high moisture content are distinctive for their flat, smooth surface with desiccation cracks in dry periods. Finally, the surface deposits (blue rectangle) appearing in the

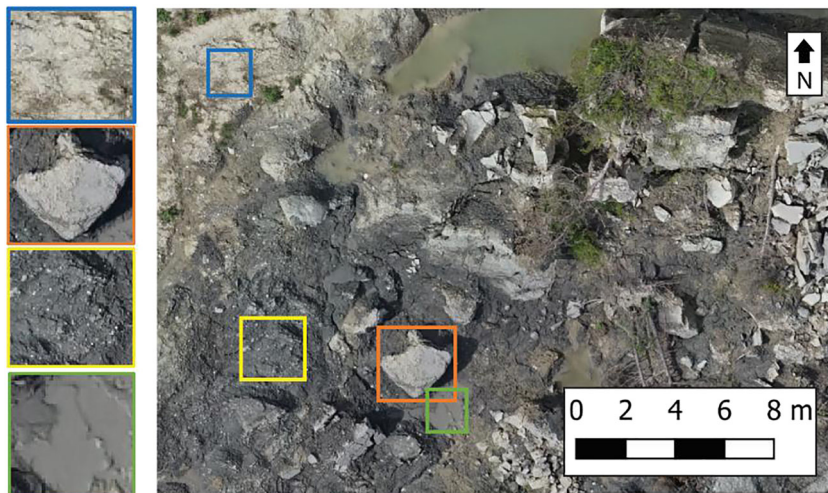


FIGURE 2 Sample image from UAV acquisition on 24 May 2018 (location in Figure 1). The four identified soils are highlighted in orange for intact clay, blue for surface deposits, green for filling clay and yellow for degraded clay. [Color figure can be viewed at [wileyonlinelibrary.com](https://onlinelibrary.wiley.com/doi/10.1002/esp.3468)]

upper part of the studied zone correspond to a thin, beige-coloured colluvial layer consisting of a mixture of clay and morainic material carried down the slope.

3 | METHODS

The flowchart of Figure 3, which was applied to evaluate clay degradation, shows the different phases of acquisition, preprocessing, processing and analysis and is detailed step by step.

3.1 | Acquisition

A vertical take-off and landing (VTOL) hexacopter (Escadrone – Six3) was used for embarking on the acquisition system. For the three flights, we used a Sony Alpha 7 hybrid Camera featuring Mirrorless full-frame 24 megapixels CMOS sensors (6000×4000 pixels) with Interchangeable Lens (35 mm F2.8 Carl Zeiss fixed lens), with a low-pass filter and on-chip phase detection. This UAV has a maximum payload of 3 kg and a flight time of 14 min. Three successive UAV acquisitions were conducted on 24 May 2018, 18 July 2018 and 24 June 2019, whose characteristics are summarized in Table 1. The acquisitions were made 2 years after the major reactivation of June 2016 and 1.5 years after January 2017 reactivation (Fiolleau et al., 2021).

3.2 | Preprocessing

To produce DEMs and orthomosaics, we applied the structure-from-motion (SfM) and multi-view stereo (MVS) methods (Remondino et al., 2014; Snavely et al., 2008; Westoby et al., 2012). We adopted the Metashape workflow (Agisoft, 2019) which consists of five steps:

1. Using the Scale Invariant Feature Transform (SIFT) algorithm (Lowe, 2004), corresponding key points are identified in the overlapping images (85% and 70% along the longitudinal and lateral flight line, respectively) and extracted to create a three-dimensional (3D) tie point cloud.

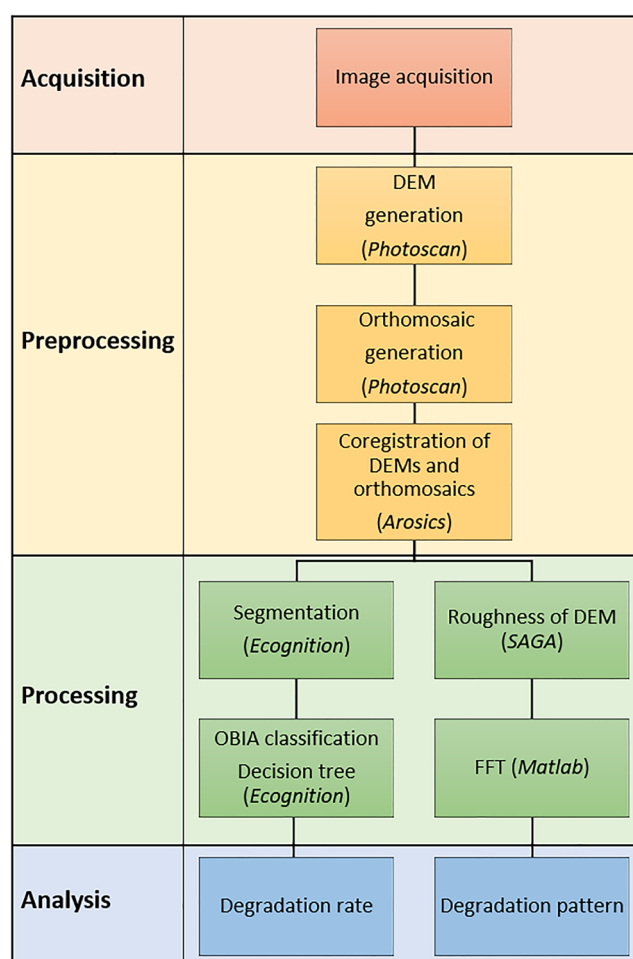


FIGURE 3 Flowchart applied to analyse the clay degradation. The software used in the preprocessing, and processing phases are in italic. [Color figure can be viewed at [wileyonlinelibrary.com](https://onlinelibrary.wiley.com/doi/10.1002/esp.3468)]

2. During georeferencing process the model is linearly transformed using seven similarity transformation parameters (three parameters for translation, three for rotation and one for scaling). The sparse cloud with image-space coordinates is transformed in an absolute coordinate system (RGF93, EPSG 2154) through the introduction of georeferenced ground-control points (GCPs) providing a better

TABLE 1 Flight parameters and weather conditions for the three unmanned aerial vehicle (UAV) acquisitions

	24 May 2018	18 July 2018	24 June 2019
Acquisition time (UTC + 1)	Three flights from 14:38 h to 16:28 h	Three flights from 11:24 h to 13:38 h	Three flights from 10:57 h to 14:24 h
Weather conditions	Sunny, cloudless sky	Sunny cloudless sky	Sunny, cloudless sky
Sun altitude (deg)	47–63	53–66	50–66
Sun azimuth (deg)	213–250	118–177	109–208
Flight elevation (m above ground)	102	66	85
Area covered (ha)	17.9	14.7	23.8
Ground resolution (mm/px)	16	11	14
Number of images	1056	1707	1485

TABLE 2 Processing characteristics for the three acquisitions

Acquisition date	24 May 2018	18 July 2018	24 June 2019
Number of GCP	24	22	46
Orthomosaic coregistration: X/Y shifts in mm (reliability)	Reference	–39/7 (89%)	–39/7 (82%)
DEM coregistration: X/Y shifts in mm (reliability)	Reference	26/18 (75%)	11/213 (87%)
Average accuracy of orthomosaic, XY/Z Rmse (mm)	93/94	99/84	106/65
DEM resolution (mm/px and pts/m ²)	65 and 241	43 and 554	55 and 340

Note: GCP, ground control point; DEM, digital elevation model; XYRmse, root-mean-square error.

accuracy (Turner et al., 2012). We implanted and surveyed landmarks using two Trimble GNSS receivers with theoretical accuracy measurements of 0.8–10 mm horizontally and 15–20 mm vertically. Twenty-four landmarks were established in 2018 before the flights in the form of painted crosses around the edge and within the study area (Appendix 2). Our goal was to achieve a density of 1.7 GCPs per hectare (Martínez-Carricondo et al., 2018). Eighteen landmarks were used as GCPs and six as control points (CPs) to estimate the accuracy of the final model for May and July 2018 (Table 2). GNSS survey was densified before the 2019 flight with 46 GCPs and 7 CPs (counting eight common GCPs for the three flights). Special attention was paid to parameters that can affect the reproducibility such as the focal length of the camera (fix 35 mm) and the location of georeferencing targets (Table 2 and Appendix 2). An iterative process of optimization allowed to refine simultaneously the exterior and interior camera orientation parameters and triangulated tie point coordinates (Clapuyt et al., 2016).

- Using a dense stereo matching algorithm, we re-constructed a dense cloud based on calculated depth maps.
- DEMs were constructed by rasterizing the dense point clouds.
- The orthomosaic was generated by merging the original red, green and blue (RGB) images projected on the DEM and transformed in the selected projection (RGF93, EPSG 2154).
- Finally, the coregistration of the series of orthomosaic and DEMs was performed using Arosics software (Scheffler et al., 2017) with the first acquisition (May 2018) as reference. This processing ensured the spatial alignment between each orthomosaic and each DEM of the series. Results and reliability of the coregistration are summarized in Table 2 with the final accuracies and resolution of the orthomosaics and DEMs, respectively.

In order to assess the quality of the images, each orthomosaic was converted to a greyscale image. Next, the grey-level co-occurrence matrix (GLCM_{ij}) was computed for eight grey levels (Haralick et al., 1973), determining how often a pixel with grey-level value *i* occurs either horizontally, vertically, or diagonally to adjacent pixels with value *j*. For each acquisition the mean contrast of the normalized GLCM matrix was computed following:

$$C_{Mean} = \sum_{i=1}^8 \sum_{j=1}^8 |i-j|^2 GLCM_{ij} \tag{1}$$

with GLCM_{ij} the grey-level co-occurrence at the position *i, j*.

The values of *C_{mean}* of 1.08, 0.42 and 0.84 were found for the 24 May 2018, 18 July 2018 and 24 June 2019 acquisitions, respectively.

3.3 | Processing

3.3.1 | Object-based image analysis (OBIA)

Image classification was performed using four layers including the RGB bands and the roughness. The objective was to classify each image into eight ground classes comprising the four previously observed types of soil (intact clay, degraded clay, filling clay and surface deposits) and four other categories corresponding to water, low vegetation (grass), high vegetation (forest) and shade.

An OBIA was conducted using eCognition software (Definiens, 2009) with two main steps: the segmentation to merge the pixels into objects and the classification of these objects.

3.3.2 | Segmentation

A multi-resolution segmentation (MRS) algorithm was applied to merge the pixels into objects (Baatz & Schape, 2000). The rationale behind this MRS approach is to minimize the average heterogeneity of image objects weighted by their size during the merging process. The algorithm has several steps of fusion going from pixels to small objects, then to larger objects considering three different parameters. The selection of these parameters (details in Appendix 1) should lead to meaningful objects (in this case: blocks of clay, vegetation areas, water ponds, etc.). The reliability of each segmentation was estimated by evaluating their accuracy manually, using QGIS (QGIS, 2020), on the same three distinctive small clay blocks for each acquisition. The accuracy of each segmentation was assessed by measuring precisely the size of three intact clay blocks of metric size and comparing the results with those of the segmentation. Accuracies of 98.9%, 80.0% and 92.0% were found for the 24 May 2018, 18 July 2018 and 24 June 2019 acquisitions, respectively.

3.3.3 | Classification

The second step of OBIA is classification. Supervised classification of each object was performed using a decision tree algorithm (Definiens, 2009). The averages and standard deviations of the series of pixels composing each object were computed for each layer (RGB and roughness) and were further used for the classification. For each image, samples of all eight classes were selected manually from field observations. The training samples correspond to 70% of this selection while the remaining 30% were used as validation samples allowing the calculation of the confusion matrices. Accuracies of 93.2%, 93.7% and 94.4% were found for the 24 May 2018, 18 July 2018 and 24 June 2019 acquisitions, respectively.

Considering both steps of OBIA (segmentation and classification), final accuracies of 92.0%, 75.0% and 86.8% were found for the 24 May 2018, 18 July 2018 and 24 June 2019 acquisitions, respectively. A more precise description of the different steps of the OBIA performed and, more particularly, of the parameterization of the decision tree is presented in Appendix 1.

3.3.4 | Roughness

Terrain roughness index (TRI)

The terrain roughness index (TRI) was computed on squares of $n \times n$ pixels² using SAGA software (Riley et al., 1999), according to:

$$TRI = \sqrt{\sum_{i=1}^n \sum_{j=1}^n (x_{ij} - x_{00})^2} \quad (2)$$

where x_{00} and x_{ij} are the elevations (in metres) of the central and neighbouring pixels, respectively. The number of pixels n was set to 15, 23 and 19, respectively, for the acquisitions of 24 May 2018, 18 July 2018 and 24 June 2019, in order to obtain a square surface of approximately 1 m².

Fast Fourier transform (FFT)

The spatial two-dimensional (2D) Fourier transforms of the TRI were calculated after applying an apodization using a Hamming window. This step aims to reduce the image edge effect on the fast Fourier transform (FFT) by windowing the signal (with a Hamming window in our case).

3.4 | Degradation analysis

The classification of images taken on three successive dates makes it possible to quantify the evolution of the surface of each material and thus the clay degradation rate (DR). According to White (2003), the erosion rate (ER) (in mol/m²/s) can be defined as:

$$ER = \frac{dM}{St} \quad (3)$$

with dM (in moles) is the loss of mass, S (in m²) the total area involved and t (in seconds) the time considered. Here, the mass of the intact blocks cannot be calculated because of potential displacements between acquisitions. Therefore, we replace the mass loss (dM) with the loss of the surface of intact clay (dS , in m²) and define the clay DR by:

$$DR = \frac{dS}{St} \quad (4)$$

with S the initial surface of intact clay (in m²).

The uncertainty on DR (in s⁻¹) was calculated using Equation (4), considering the combined effect of the segmentation and the classification steps. The degradation process has also been studied through the analysis of surface roughness calculated from DEMs (Goetz et al., 2014; LaHusen et al., 2016).

4 | RESULTS

The degradation of the clay material was analysed at three different spatial scales: over the whole study area (about 15 ha), over two intermediate sized areas (75 × 75 m²) and metric-sized blocks.

4.1 | Analysis of the study area

The orthophotos on the three dates are shown in Figure 4. They were acquired under close sunny and cloudless sky conditions (Table 1). They show variations in contrast C_{mean} (Table 1), with a value twice lower for the 24 July 2018 acquisition due to sun azimuth (< 177°, Table 1). The corresponding three classified images (Figure 4, right column) show a similar spatial pattern for the eight ground classes. An error of classification appears in the lower part of the July 2018 image (red ellipse in Figure 4b) where a significant area of degraded clay was misinterpreted as filling clay. Similar minor misclassifications were identified in small areas of the images.

Quantifying the areas covered by the eight classes (Figure 5a) gives the following decreasing order: degraded clay (25–32%), high

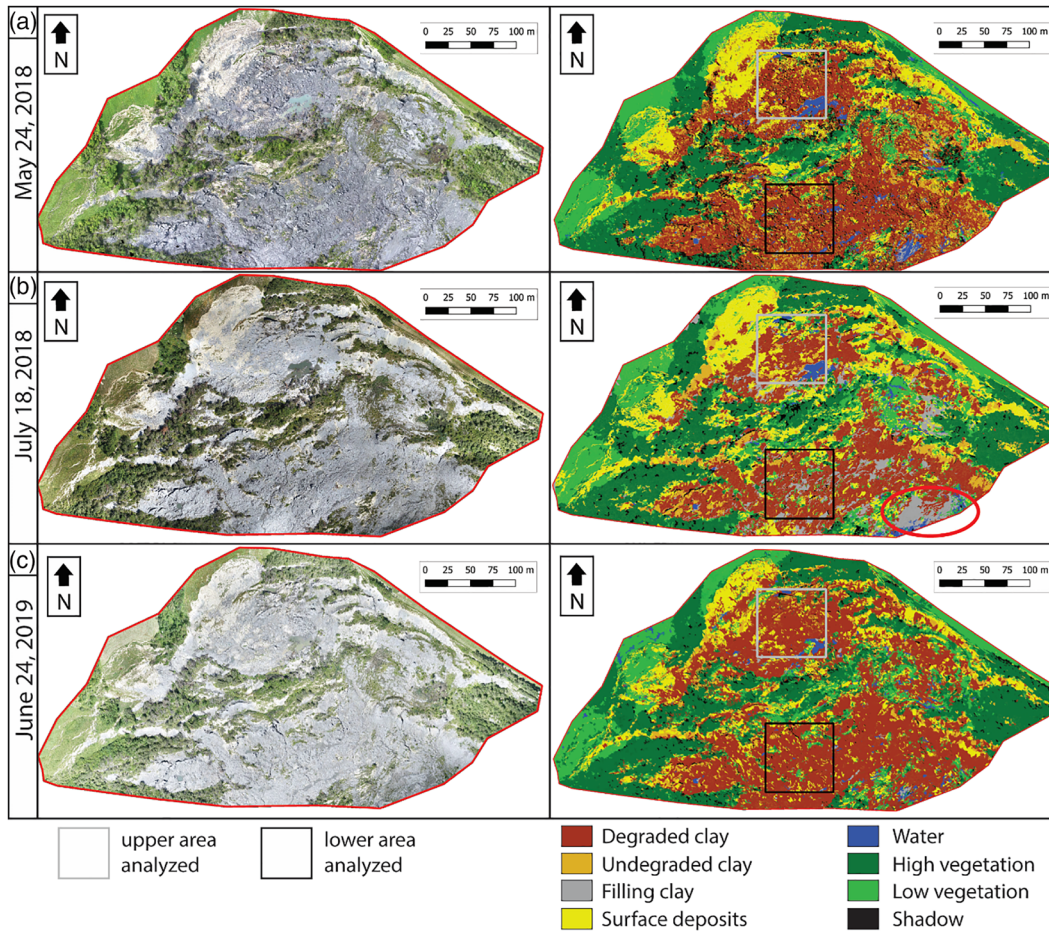
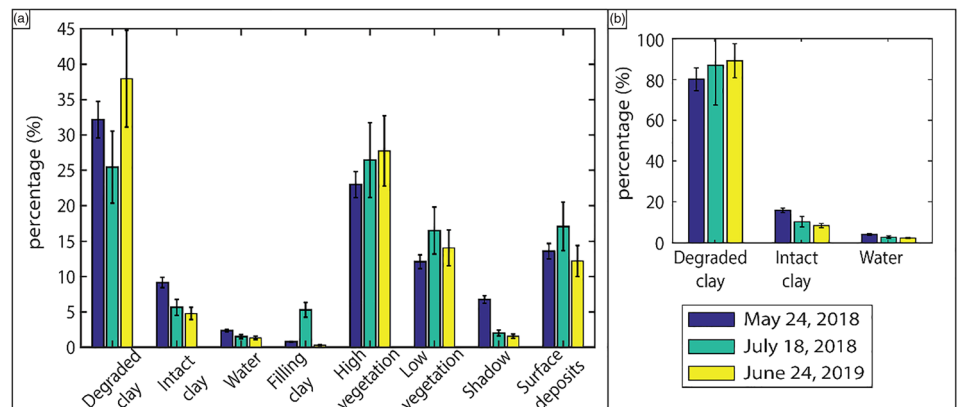


FIGURE 4 Orthophotos (left) and classifications (right) of acquisitions of (a) 24 May 2018, (b) 18 July 2018 and (c) 24 June 2019. The grey and black squares correspond to the upper and lower intermediate-size close-ups investigated, respectively. The red ellipse shows an area of filling clay misinterpreted by the 18 July 2018 classification. [Color figure can be viewed at wileyonlinelibrary.com]

FIGURE 5 Area covered by each class (in percentage) in the study area. (a) Area covered by each of the eight initial classes. (b) Area covered by the three classes of degraded clay, intact clay and water after merging of the degraded clay class (see text) and without considering the vegetation and shadow classes. [Color figure can be viewed at wileyonlinelibrary.com]



vegetation (23–27.7%), low vegetation and surface deposits (both 12–17%), intact clay (4.8–9.2%), and finally, filling clay, water, and shade (0.3–6.7% in total). At the time of acquisition, the percentage of degraded clay is much higher than that of intact clay. While some classes (intact clay, water) appear to have a regular evolution, others (shade, degraded clay, etc.) show sharp variations from one date to another. In particular, the shadow area is four times larger in May 2018 image than in the other two. The main differences are in the high vegetation areas, which induced more shadows considering the lower sun altitude during the May 2018 acquisition (Table 1).

However, these variations between these two classes (high vegetation and shadow) do not affect the overall interpretation of the others.

As expected, the percentage of intact clay steadily decreases over time (from 9.2 ± 0.7 to $5.7 \pm 1.1\%$). However, this decrease is not offset, as would have been assumed, by an increase in the percentage of degraded clay. Indeed, we observed a decay of degraded clay from 32 ± 2.6 to $25 \pm 5.1\%$ between May and July 2018 (Figure 5a). This discrepancy is mainly due to the classification error mentioned earlier (red ellipse in Figure 4), leading to an erroneous increase (decrease) in the percentage of filling clay (degraded clay) between May and July

2018 (Figure 5a). An additional reason for this discrepancy is a possible confusion between degraded clay and surface deposits. Indeed, the surface deposits, which generally lie on the degraded clay, may be very thin and then difficult to distinguish from degraded clays. Because of these misclassifications, we decided to merge these three classes (filling clay, surface deposits, and degraded clay) into a single class, namely degraded clay. The area evolution of the three classes of degraded clay, intact clay and water is shown in Figure 5(b), where the other classes of vegetation and shadow were removed. The decrease in the percentage of intact clay area is now accompanied by a corresponding increase in that of degraded clay, while the main change in water-covered area is a decrease between May and July 2018, likely resulting from summer evaporation (see Discussion section).

4.2 | Detailed analysis of intermediate sized areas

4.2.1 | Degradation rate (DR) analysis

Two square areas (75 m × 75 m) located in the upper and lower parts of the study area (see location in Figure 4) were selected in order to investigate the clay degradation evolution in more detail. The corresponding photographs and classification images are shown in Figure 6(a,b) for the three acquisition dates and the four classes (intact clay, degraded clay, water and others) in the upper and lower areas. As well as for the whole study area, an increase in degraded clay with time is observed in both areas over the complete period (Figure 7a,b), associated with a decrease in intact clay in the upper ($5.3 \pm 1.8\%$) and lower ($11.2 \pm 1.3\%$) areas, respectively. The water percentage

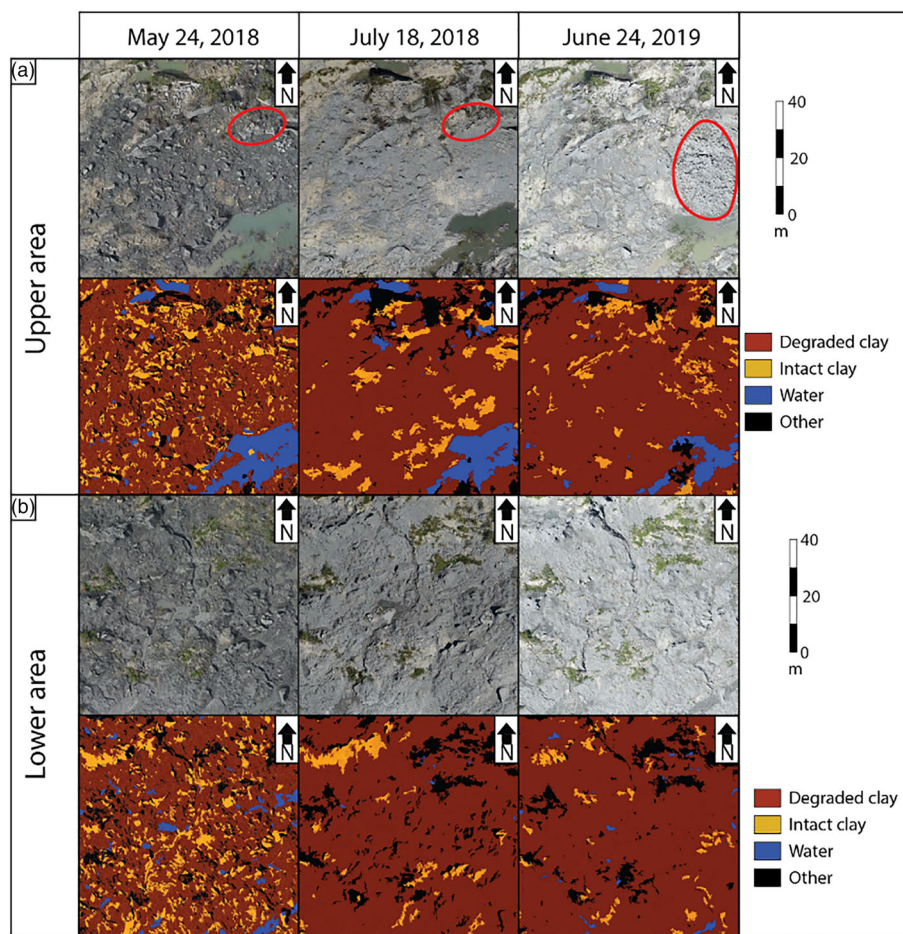


FIGURE 6 Classification for the two intermediate-size areas. (a) Photographs and corresponding classifications for the upper area. The block failure observed between July 2018 and June 2019 is highlighted with a red ellipse, before and after the failure. (b) Photograph and corresponding classification for the lower area. [Color figure can be viewed at wileyonlinelibrary.com]

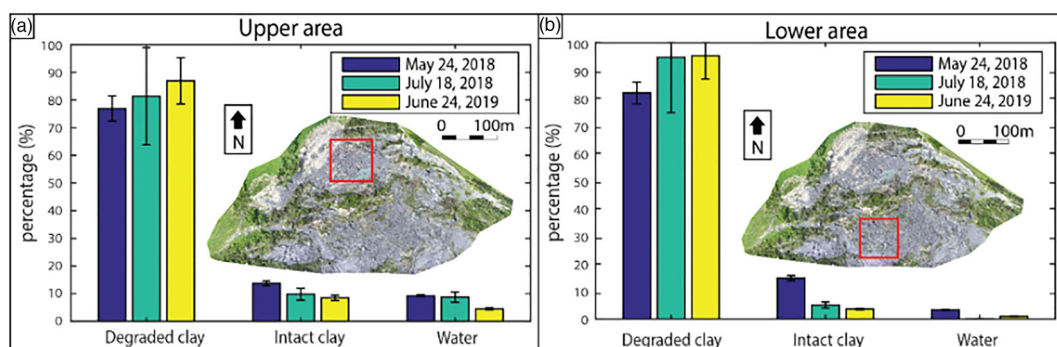


FIGURE 7 Percentage of area covered by degraded clay, intact clay and water for the (a) upper and (b) lower areas (red square). [Color figure can be viewed at wileyonlinelibrary.com]

variations are limited and may affect slightly the values in degraded clay, particularly in the upper area. The location of a block of a few cubic metres that broke between July 2018 and June 2019 is shown in Figure 6(a, red ellipse), with the debris area after the block failure depicted in the June 2019 photograph (Figure 6a, red ellipse).

The rate of clay degradation DR was calculated for the upper, lower and whole study areas (Table 3), using Equation (4). Over the entire period, DR appears twice as high in the lower area than in the upper area, with values of 0.69 yr^{-1} and 0.35 yr^{-1} , respectively, with uncertainty ranging from 17% to 42%. Considering the intermediate 18 July 2018 acquisition makes it possible to compute two DR values over the study period. In all areas, clay degradation is 10 times faster between May and July 2018 than between July 2018 and June 2019. These two intermediate DR values (Table 3) are however affected by a very high uncertainty (close to or above 100%), which is probably related to the poor contrast of the July 2018 acquisition and raises suspicion about the DR values computed. Therefore, we will only consider the DR values over the whole period in the following.

4.2.2 | Analysis of morphological features

Roughness was analysed in terms of amplitude and spectral characteristics to further investigate the clay degradation processes.

Figure 8(a) shows the optical images of the upper and lower areas for each acquisition, while Figure 8(b,c) display the roughness images and their spectral analysis, respectively. The mean roughness was computed for each image (values in Table 4). The roughness (Figure. 8b; Table 4) is 18% to 25% higher in the upper area for all acquisitions, indicating a blockier material than in the lower area. This decrease in roughness towards the lower area corresponds to the degradation of blocks into mounds.

The mean roughness decreases drastically in the two areas (by about 4.5 times, Table 4) between May and July 2018 in both zones, before increasing slightly (by about 1.5 times) between July 2018 and June 2019.

The spectral analysis (Figure 8c) shows that the upper area is distinguished from the lower area by a higher roughness at high wavenumbers (short wavelengths), suggesting the presence of numerous small blocks. Preferential orientations appear in the 2D Fourier

TABLE 4 Mean roughness values over all wavenumbers

Acquisition date	Mean roughness (mm)		
	24 May 2018	18 July 2018	24 June 2019
Upper area	124	26	43
Lower area	98	22	35

TABLE 3 Degradation rates (DRs) calculated from Equation (4) over the upper, lower and whole study areas, between May and July 2018, between July 2018 and June 2019, and over the entire period

Studied area	DR ± uncertainty (yr^{-1})		
	May–July 2018 (55 days)	July 2018–June 2019 (341 days)	May 2018–June 2019 (396 days)
Upper area	1.88 ± 1.59	0.14 ± 0.37	0.35 ± 0.15
Lower area	4.36 ± 1.19	0.30 ± 0.39	0.69 ± 0.12
Study area	2.31 ± 1.66	0.20 ± 0.42	0.43 ± 0.16

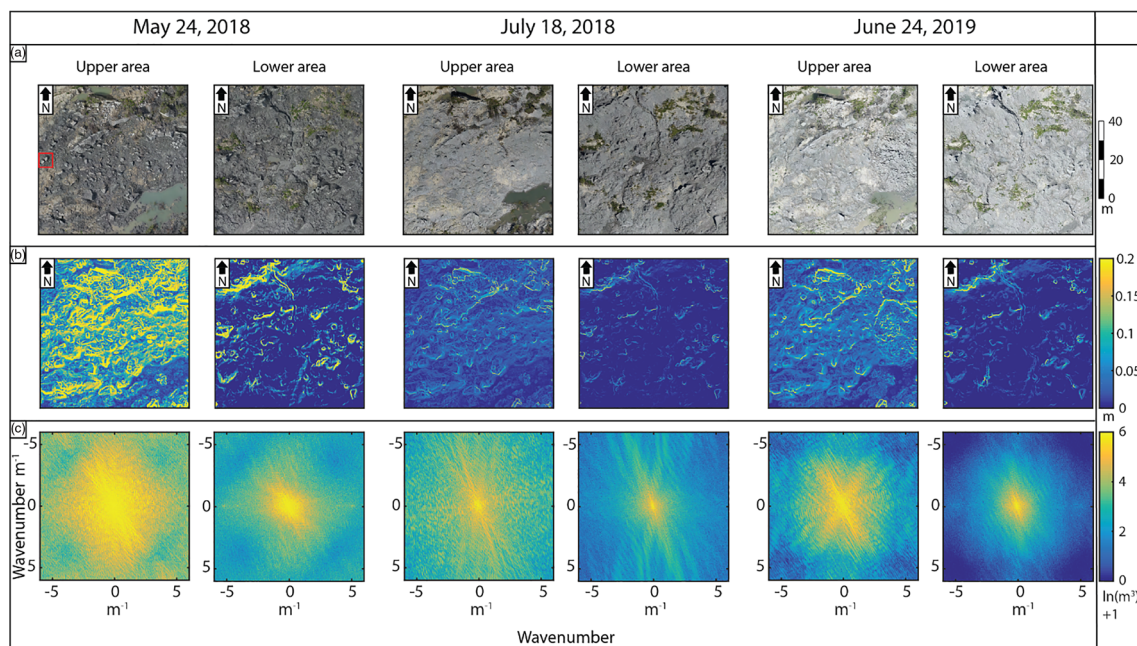


FIGURE 8 Roughness of the upper and lower areas (grey and black squares in Figure 3, respectively) for the three acquisitions. (a) Orthophotos. The red square delimits the zone analysed in Figure 10. (b) Roughness (m) subtracted from its average. (c) Two-dimensional Fourier transform of the roughness (wavenumber domain) [Color figure can be viewed at wileyonlinelibrary.com]

transform (Figure 8c), especially in the upper region for the last two acquisitions, with the main direction N330°–340°. This orientation, which is perpendicular to the actual one, corresponds to scarps oriented N60° to N70°, which are visible in the roughness images (Figure 8b). The roughness Fourier transform also highlights other secondary orientations (N30° and N70°), corresponding to structures parallel to the slope and lateral scarps and oriented N120° to N160°.

To better characterize the roughness spectral changes, their average 2D Fourier transform and associated standard deviation were calculated by averaging 10 equally azimuthally distributed profiles (each 18°) for each acquisition in the upper and lower areas (Figure 9a,b). Considering the temporal evolution, a strong decrease in the roughness (Figure 9, by a factor of three, Table 4) is visible over the entire period. This observation is consistent with the high DR observed previously. First, a general decrease is observed between May and July 2018 for all wavenumbers (by a factor of 4.5 on average, Table 4), with a stronger decay for wavenumbers smaller than 1 m⁻¹. Second, the roughness still decreases between July 2018 and June 2019 for the large wavenumbers, but increases for wavenumbers lower than 2.8 and 1.5 m⁻¹ (corresponding wavelengths larger than 0.36 m and 0.66 m) in the upper and lower areas, respectively.

Figure 9 shows a slightly different wavelength distribution between the two areas. In the upper area, the significant presence of blocks greater than 2 m (wavenumber: 0.5 m⁻¹) creates a bulge in the distribution (Figure 9a, black dashed lines), followed by a more linear decrease toward shorter wavelengths. In the lower area, the bulge in the distribution is slightly less pronounced (smoother distribution) and wider. This highlights the presence of smaller blocks (wavenumber: 1 m⁻¹; black dashed lines in Figure 9b) and in a smaller amount than in the upper area, before reaching a more linear decrease.

4.3 | Analysis at the scale of the blocks

To better understand the previous results and the degradation mechanisms, we studied the evolution of two close blocks P1 and P2 located in the upper zone (Figure 10a). The two blocks are of several metres in size with a volume of 2.6 m³ and 4.9 m³, respectively. The degradation process of the blocks took place in two stages. First, a strong decay in roughness occurred between May and July 2018 (Figure 10c,f). This decrease results from the smoothing of the shape of the two blocks

(Figure 10b,e). Then, between July 2018 and June 2019, the northern edge of the blocks broke off (Figure 10c,f), giving way to smaller blocks (1.3 m³ and 3.3 m³ for P1 and P2, respectively) and increasing the roughness between the two dates. In the spectral domain (Figure 10d,g), the same evolution is observed with first a Fourier amplitude reduction of at least two, reaching six for some wavelengths, between May and July 2018. Then the Fourier amplitude increased by a factor of about two between July 2018 and June 2019 for wavenumbers smaller than 4 m⁻¹ (wavelength > 0.25 m). This pattern is similar to that observed for the square of 75 m side length in the upper area (Figure 9).

5 | DISCUSSION

The images and the roughness extracted from three UAV acquisitions were used to classify the materials at the surface of the study area located in the upper part of the Harmalière landslide. The identification of intact and degraded clay areas made it possible to quantify the DR (Table 3) over the whole study area and in two smaller areas (75 m × 75 m) and to monitor the evolution of this quantity over time.

Over the entire period (24 May 2018–24 June 2019), DR is twice higher in the lower area (0.75 yr⁻¹, Table 3) than in the upper area (0.38 yr⁻¹, Table 3). This indicates that the degrading process is more active in the already weathered blocks. The mean value of DR over the study area (0.43 yr⁻¹) suggests that the degradation process (if steady) would take a few years to completely transform the blocks into mounds of degraded clay. This conclusion must, however, be tempered by the short monitoring time (just over 1 year), the small number of acquisitions and the relatively high uncertainty due to the acquisition conditions. Further acquisitions are required to draw firm conclusions.

The roughness analysis also highlights a difference between the upper and lower areas, with a higher roughness (about 1.25 times higher) in the upper area. Further down the slope, the blocks are smoother and evolve into mounds. An interesting point is the temporal evolution of the roughness parameters over the study period, with a significant decrease in roughness between 24 May 2018 and 18 July 2018 (by a factor of 4.5) and a slight increase between 18 July 2018 and 24 June 2019 (by a factor of about 1.6). As shown by the study at

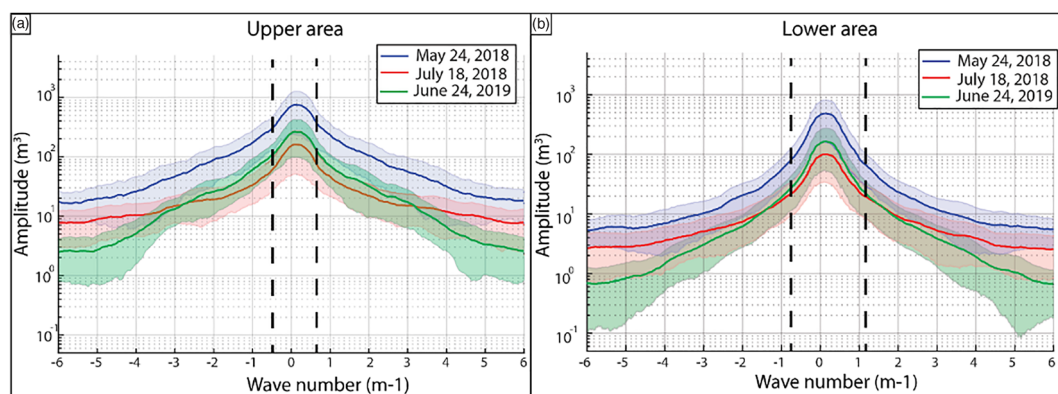


FIGURE 9 Roughness study. Average 2D Fourier transform (FFT2) profiles (10 profiles) for each acquisition date and its standard deviation (shaded zone). (a) Upper area. (b) Lower area. The dashed lines highlight the bulges (bounded by the first significant gradient variation in 24 May 2018). [Color figure can be viewed at wileyonlinelibrary.com]

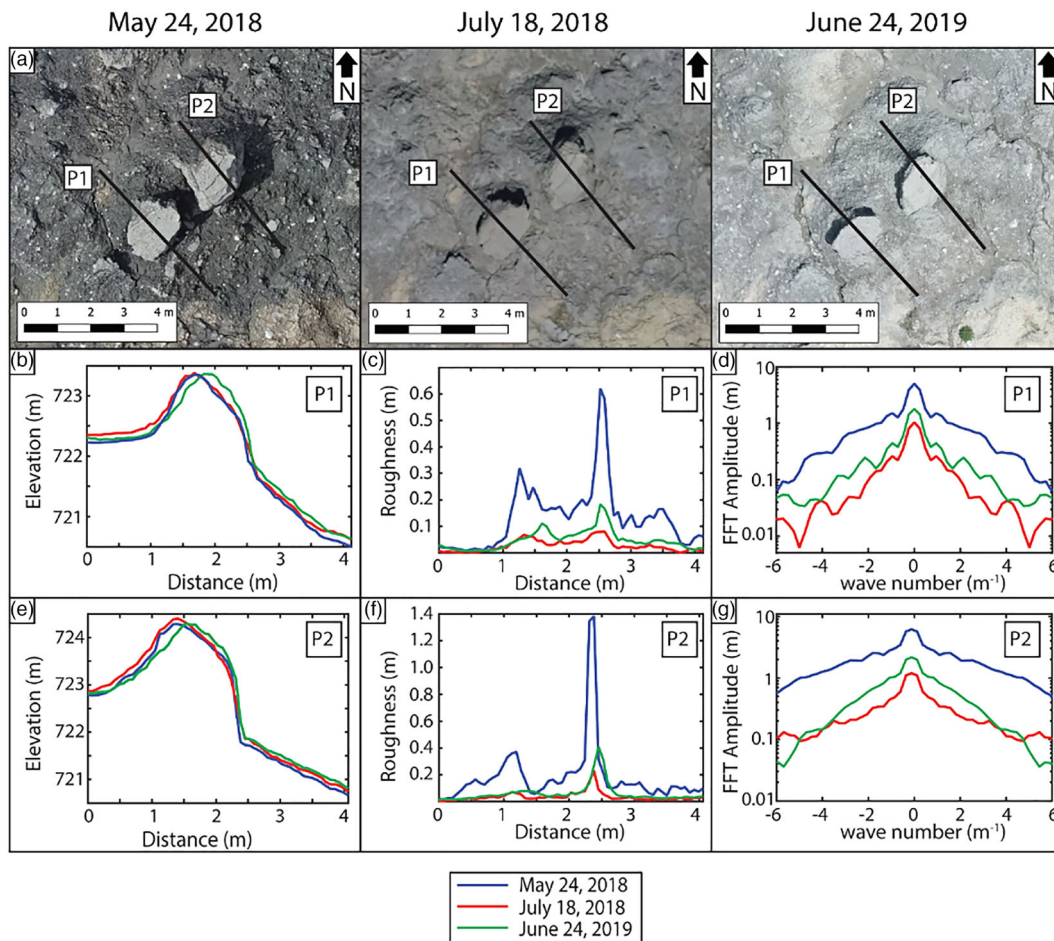
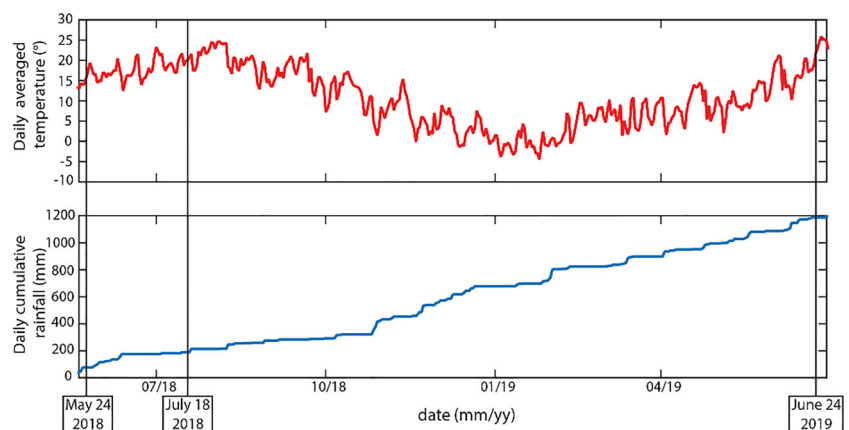


FIGURE 10 Close-up on two plurimetric blocks in the upper area (location in Figure 8). (a) Orthophotos of the blocks for the three dates. (b) Topographic profile P1. (c) Roughness profile P1. (d) Fourier transform of the roughness of P1. (e) Topographic profile P2. (f) Roughness profile P2. (g) Fourier transform of the roughness of P2. [Color figure can be viewed at wileyonlinelibrary.com]

FIGURE 11 Daily averaged temperature (top) and daily cumulative rainfall (bottom) during the monitoring period. Black lines indicate the three acquisition dates. Data are provided by a meteorological station (French National Meteorological Service), located in Monestier-de-Clermont, 3 km west of the site and at a similar altitude. [Color figure can be viewed at wileyonlinelibrary.com]



the metre scale, this surprising roughness rise between the last two dates can be explained by the breakage of blocks. The strong decrease in roughness between the first two acquisitions supports the DR results, with a more pronounced degradation during this period.

Looking at the meteorological data at a station located 3 km west of the site (Figure 11), this first period (between 24 May and 18 July 2018) was relatively hot (temperature between 15°C and 25°C), with rainfalls in early June reaching a total amount of about 150 mm. The conjunction of hot temperatures with significant precipitation has presumably generated swelling and shrinkage cycles, leading to fast degradation of the clay blocks and a decrease in roughness, as shown by

Meisina (2004). The period between the two last acquisitions (July 2018–June 2019) was relatively rainy (precipitation totalling up to 1000 mm, with a two months period from December 2018 to January 2019 during which temperature oscillated between positive and negative values). The block breakages are interpreted as the combined effect of freeze–thaw cycles in winter and shrink–swell cycles, with the effect of the former predominating in a generally colder period (Pardini et al., 1996). Analyses of the two small blocks (Figure 10) highlight the same degradation processes which, depending on the climatic conditions, alternate between smoothing and then breaking into smaller pieces.

6 | CONCLUSIONS

Optical images acquired from an UAV were used to analyse the degradation process affecting clayey materials in the Harmalière landslide, French Western Alps. This landslide presents a sliding mechanism in its upper part. Clayey blocks, metric to several metres in size, are progressively degraded while being transported down-slope, leading to a flow-like behaviour in the lower part of the landslide. In a landslide context, two factors contribute to the degradation of the clay at the surface: landslide-induced deformation and weathering. These processes are closely related since landslide-induced deformation tends, for example, to devegetate and to generate new fractures in the mobilized areas which favours surface weathering, and surface weathering decreases material competence, facilitating the solid–fluid transition and thus displacement. In this study, we focused on the weathering process since no displacement was observed during the monitoring period. The degradation process in the upper part of the landslide was analysed using two approaches. First, OBIA was applied to classify three orthomosaics acquired over a period of around 1 year into eight ground classes comprising four types of soil (intact clay, degraded clay, filling clay and surface deposits). The evolution of the soil areas with time allowed us to compute the DR of the intact clay. Second, the degradation pattern was studied from the evolution of the TRI and its spectral characteristics. Although limited to a relatively short period (14 months, three acquisitions), this methodological study combining two approaches highlighted an average rate of degradation of about 0.4 yr^{-1} accompanied by a strong decrease in roughness (about three times). The DR is twice higher for the lower area, indicating that degradation processes are more active in the already weathered blocks. The observed degradation probably mainly results from weathering, as no global movement was detected in the images.

The small number of acquisitions and the low contrast of the July 2018 acquisition highlighted the importance of the acquisition conditions (frequency, acquisition hour, cloud cover, camera settings, etc.) and measurements repeatability to obtain comparable images and finally more robust results. However, even within the limitations of this preliminary study, the methods used showed promising results, highlighting the usefulness of UAV acquisitions to monitor degradation patterns in the context of slope instability. In future studies, the application of this methodology on longer time-series with shorter revisit times is required to produce more robust interpretations, especially to obtain more precise estimates of the DRs in different zones. In addition, image correlation could provide high-resolution (centimetre-scale) displacement fields and would allow linking displacement and degradation, leading to a better understanding of the degradation processes that ultimately drive the evolution of the landslide mechanism.

ACKNOWLEDGEMENTS

The authors thank the Editor-in-Chief, Associate Editor and reviewers who provided insightful comments on this article.

The authors acknowledge the financial support from the French VOR federative structure, the French national C2ROP project, the French National Research Agency in the framework of the Investissements d'Avenir programme (ANR-15-IDEX-02, CDPRISK), and the LabEx OSUG@2020 (ANR10 LABX56).

CONFLICT OF INTEREST

The authors have no conflicts of interest to declare.

AUTHOR CONTRIBUTIONS

Fiolleau Sylvain: conceptualization; methodology (including methodological development); writing – initial draft; writing – reviewing and editing. Jongmans Denis: funding acquisition; writing – reviewing and editing. Bièvre Grégory: funding acquisition; writing – reviewing and editing. Chambon Guillaume: funding acquisition; writing – reviewing and editing. Michel Olivier: methodology (including methodological development); writing – reviewing. Borgniet Laurent: investigation (e.g. data collection).

DATA AVAILABILITY STATEMENT

The data that support the findings of this study are available from the corresponding author upon reasonable request.

ORCID

Sylvain Fiolleau  <https://orcid.org/0000-0001-6269-8676>

Laurent Borgniet  <https://orcid.org/0000-0001-9408-031X>

REFERENCES

- Agisoft, L.L.C. (2019) *Agisoft metashape user manual*. Russia: Professional edition.
- Batz, M. & Schape, A. (2000) Multiresolution segmentation: An optimization approach for high quality multi-scale image segmentation. In: Strobl, J., Blaschke, T. & Griesbner, G. (Eds.) *Angewandte Geographische Informationsverarbeitung*. Karlsruhe, Germany: Wichmann Verlag, pp. 12–23.
- Baum, R.L., Messerich, J. & Fleming, R.W. (1998) Surface deformation as a guide to kinematics and three-dimensional shape of slow-moving, clay-rich landslides, Honolulu, Hawaii. *Environmental & Engineering Geoscience*, 4(3), 283–306. Available from: <https://doi.org/10.2113/gsegeosci.v3.283>
- Bertello, L., Berti, M., Castellaro, S. & Squarzone, G. (2018) Dynamics of an active earthflow inferred from surface wave monitoring. *Journal of Geophysical Research: Earth Surface*, 123(8), 1811–1834. Available from: <https://doi.org/10.1029/2017JF004233>
- Berti, M., Corsini, A. & Daehne, A. (2013) Comparative analysis of surface roughness algorithms for the identification of active landslides. *Geomorphology*, 182, 1–18. Available from: <https://doi.org/10.1016/j.geomorph.2012.10.022>
- Besson, L. (1996) *Les risques naturels en montagne*. France: Artès-publialp.
- Bièvre, G. & Crouzet, C. (2021) Multi-proxy analysis of boreholes in remolded quaternary paraglacial deposits (Avignonet landslide, French Western Alps). *Engineering Geology*, 286, 106073. Available from: <https://doi.org/10.1016/j.enggeo.2021.106073>
- Bièvre, G., Jongmans, D., Winiarski, T. & Zumbo, V. (2012) Application of geophysical measurements for assessing the role of fissures in water infiltration within a clay landslide (Trièves area, French Alps). *Hydrological Processes*, 26(14), 2128–2142. Available from: <https://doi.org/10.1002/hyp.7986>
- Blaschke, T. (2010) Object based image analysis for remote sensing. *ISPRS Journal of Photogrammetry and Remote Sensing*, 65(1), 2–16. Available from: <https://doi.org/10.1016/j.isprsjprs.2009.06.004>
- Bonetti, S. & Porporato, A. (2017) On the dynamic smoothing of mountains. *Geophysical Research Letters*, 44(11), 5531–5539. Available from: <https://doi.org/10.1002/2017GL073095>
- Booth, A.M., McCarley, J.C. & Nelson, J. (2020) Multi-year, three-dimensional landslide surface deformation from repeat lidar and response to precipitation: Mill gulch earthflow, California. *Landslides*, 17(6), 1283–1296. Available from: <https://doi.org/10.1007/s10346-020-01364-z>
- Carrière, S., Bièvre, G., Jongmans, D., Chambon, G., Bellot, H. & Lebourg, T. (2018) Measurement of geophysical parameters on clay samples at

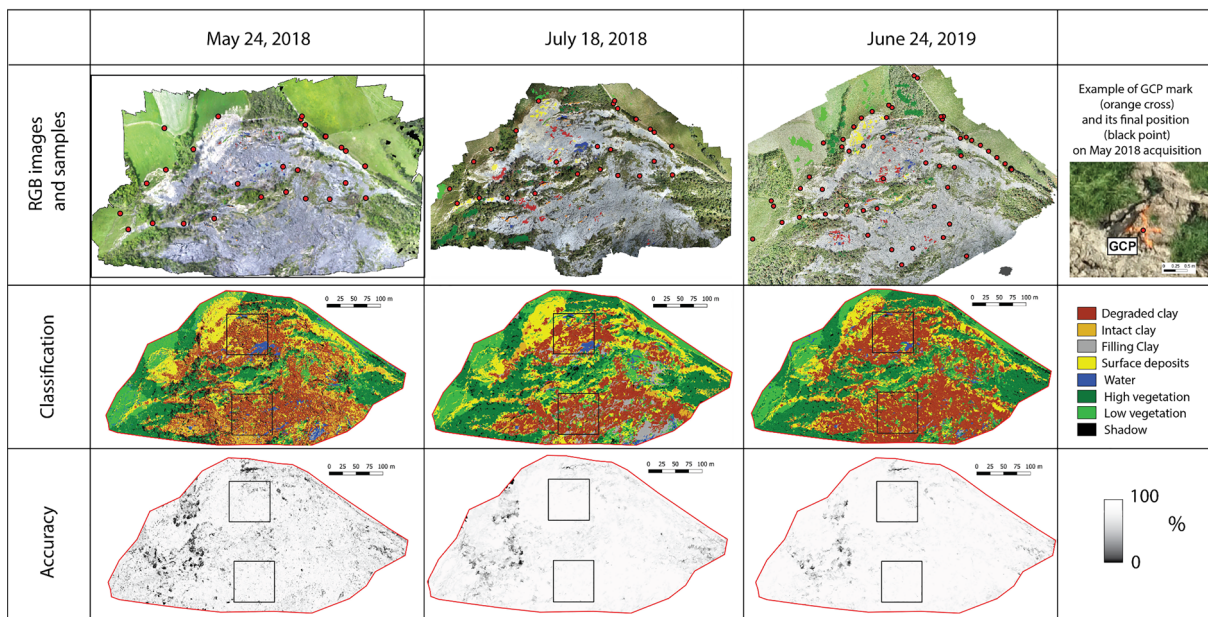
- the solid–fluid transition. *Near Surf Geophys*, 16(1), 23–37. Available from: <https://doi.org/10.3997/1873-0604.2017039>
- Casagli, N., Frodella, W., Morelli, S., Tofani, V., Ciampalini, A., Intrieri, E., Raspini, F., Rossi, G., Tanteri, L. & Lu, P. (2017) Spaceborne, UAV and ground-based remote sensing techniques for landslide mapping, monitoring and early warning. *Geoenvironmental Disasters*, 4(1), 9. Available from: <https://doi.org/10.1186/s40677-017-0073-1>
- Chae, B.G., Ichikawa, Y., Jeong, G.C., Seo, Y.S. & Kim, B.C. (2004) Roughness measurement of rock discontinuities using a confocal laser scanning microscope and the Fourier spectral analysis. *Engineering Geology*, 72(3–4), 181–199. Available from: <https://doi.org/10.1016/j.enggeo.2003.08.002>
- Chambers, J.E., Wilkinson, P.B., Kuras, O., Ford, J.R., Gunn, D.A., Meldrum, P.I., Pennington, C.V.L., Weller, A.L., Hobbs, P.R.N. & Ogilvy, R.D. (2011) Three-dimensional geophysical anatomy of an active landslide in Lias group mudrocks, Cleveland Basin, UK. *Geomorphology*, 125(4), 472–484. Available from: <https://doi.org/10.1016/j.geomorph.2010.09.017>
- Chang, K.-T., Liu, J.-K. & Wang, C.-I. (2012) An object-oriented analysis for characterizing the rainfall-induced shallow landslide. *Journal of Marine Science and Technology (Taiwan)*, 20, 647–656. Available from: <https://doi.org/10.6119/JMST-012-0430-2>
- Cignetti, M., Godone, D., Wrzesniak, A. & Giordan, D. (2019) Structure from motion multisource application for landslide characterization and monitoring: The Champlas du col case study, Sestriere, North-Western Italy. *Sensors*, 19(10), 2364. Available from: <https://doi.org/10.3390/s19102364>
- Clapuyt, F., Vanacker, V. & Van Oost, K. (2016) Reproducibility of UAV-based earth topography reconstructions based on structure-from-motion algorithms. *Geomorphology*, 260, 4–15. Available from: <https://doi.org/10.1016/j.geomorph.2015.05.011>
- Comert, R., Avdan, U., Gorum, T. & Nefeslioglu, H.A. (2019) Mapping of shallow landslides with object-based image analysis from unmanned aerial vehicle data. *Engineering Geology*, 260, 105264. Available from: <https://doi.org/10.1016/j.enggeo.2019.105264>
- Definiens, A.G. (2009) *Definiens eCognition developer 8 user guide*. Munchen, Germany: Definiens AG.
- Deilami, K. & Hashim, M. (2011) Very high resolution optical satellites for DEM generation: A review. *European Journal of Scientific Research*, 49, 542–554.
- Eker, R., Aydın, A. & Hübl, J. (2017) Unmanned aerial vehicle (UAV)-based monitoring of a landslide: Gallenzerkogel landslide (Ybbs-Lower Austria) case study. *Environmental Monitoring and Assessment*, 190(1), 28. Available from: <https://doi.org/10.1007/s10661-017-6402-8>
- Evans, I.S. (2006) Local aspect asymmetry of mountain glaciation: A global survey of consistency of favoured directions for glacier numbers and altitudes. *Geomorphology*, 73(1–2), 166–184. Available from: <https://doi.org/10.1016/j.geomorph.2005.07.009>
- Fiolleau, S., Jongmans, D., Bièvre, G., Chambon, G., Lacroix, P., Helmstetter, A., Wathélet, M. & Demierre, M. (2021) Multi-method investigation of mass transfer mechanisms in a retrogressive clayey landslide (Harmalière, French Alps). *Landslides*, 18(6), 1981–2000. Available from: <https://doi.org/10.1007/s10346-021-01639-z>
- Ghorbanzadeh, O., Shahabi, H., Crivellari, A., Homayouni, S., Blaschke, T. & Ghamisi, P. (2022) Landslide detection using deep learning and object-based image analysis. *Landslides*, 19(4), 929–939. Available from: <https://doi.org/10.1007/s10346-021-01843-x>
- Giordan, D., Allasia, P., Manconi, A., Baldo, M., Santangelo, M., Cardinali, M., Corazza, A., Albanese, V., Lollino, G. & Guzzetti, F. (2013) Morphological and kinematic evolution of a large earthflow: The Montaguto landslide, southern Italy. *Geomorphology*, 187, 61–79. Available from: <https://doi.org/10.1016/j.geomorph.2012.12.035>
- Goetz, J.N., Bell, R. & Brenning, A. (2014) Could surface roughness be a poor proxy for landslide age? Results from the Swabian Alb, Germany. *Earth Surface Processes and Landforms*, 39(12), 1697–1704. Available from: <https://doi.org/10.1002/esp.3630>
- Graham, J. & Shields, D.H. (1985) Influence of geology and geological processes on the geotechnical properties of a plastic clay. *Engineering Geology*, 22(2), 109–126. Available from: [https://doi.org/10.1016/0013-7952\(85\)90042-0](https://doi.org/10.1016/0013-7952(85)90042-0)
- Haralick, R.M., Shanmugam, K. & Dinstein, I. (1973) Textural features for image classification. *IEEE Transactions on Systems, Man, and Cybernetics*, SMC-3(6), 610–621. Available from: <https://doi.org/10.1109/TSMC.1973.4309314>
- Heleno, S., Matias, M., Pina, P. & Sousa, A.J. (2016) Semiautomated object-based classification of rain-induced landslides with VHR multispectral images on Madeira Island. *Natural Hazards and Earth System Sciences*, 16(4), 1035–1048. Available from: <https://doi.org/10.5194/nhess-16-1035-2016>
- Hölbling, D., Eisank, C., Albrecht, F., Vecchiotti, F., Friedl, B., Weinke, E. & Kociu, A. (2017) Comparing manual and semi-automated landslide mapping based on optical satellite images from different sensors. *Geosciences*, 7(2), 37. Available from: <https://doi.org/10.3390/geosciences7020037>
- Hungr, O., Leroueil, S. & Picarelli, L. (2014) The Varnes classification of landslide types, an update. *Landslides*, 11(2), 167–194. Available from: <https://doi.org/10.1007/s10346-013-0436-y>
- Hurst, M.D., Mudd, S.M., Attal, M. & Hilley, G. (2013) Hillslopes record the growth and decay of landscapes. *Science*, 341(6148), 868–871. Available from: <https://doi.org/10.1126/science.1241791>
- Jongmans, D., Bièvre, G., Renalier, F., Schwartz, S., Bearez, N. & Orengo, Y. (2009) Geophysical investigation of a large landslide in glaciolacustrine clays in the Trièves area (French Alps). *Engineering Geology*, 109(1–2), 45–56. Available from: <https://doi.org/10.1016/j.enggeo.2008.10.005>
- Lacroix, P., Berthier, E. & Maquerhua, E.T. (2015) Earthquake-driven acceleration of slow-moving landslides in the Colca Valley, Peru, detected from Pléiades images. *Remote Sensing of Environment*, 165, 148–158. Available from: <https://doi.org/10.1016/j.rse.2015.05.010>
- Lacroix, P., Bièvre, G., Pathier, E., Knies, U. & Jongmans, D. (2018) Use of Sentinel-2 images for the detection of precursory motions before landslide failures. *Remote Sensing of Environment*, 215, 507–516. Available from: <https://doi.org/10.1016/j.rse.2018.03.042>
- LaHusen, S.R., Duvall, A.R., Booth, A.M. & Montgomery, D.R. (2016) Surface roughness dating of long-runout landslides near Oso, Washington (USA), reveals persistent postglacial hillslope instability. *Geology*, 44(2), 111–114. Available from: <https://doi.org/10.1130/G37267.1>
- Lowe, D.G. (2004) Distinctive image features from scale-invariant keypoints. *International Journal of Computer Vision*, 60(2), 91–110. Available from: <https://doi.org/10.1023/B:VISI.0000029664.99615.94>
- Lucieer, A., Jong, S.M.D. & Turner, D. (2014) Mapping landslide displacements using structure from motion (SfM) and image correlation of multi-temporal UAV photography. *Progress in Physical Geography: Earth and Environment*, 38(1), 97–116. Available from: <https://doi.org/10.1177/0309133313515293>
- Ma, J., Tang, H., Liu, X., Hu, X., Sun, M. & Song, Y. (2017) Establishment of a deformation forecasting model for a step-like landslide based on decision tree C5.0 and two-step cluster algorithms: A case study in the three gorges reservoir area, China. *Landslides*, 14(3), 1275–1281. Available from: <https://doi.org/10.1007/s10346-017-0804-0>
- Ma, S., Xu, C., Shao, X., Zhang, P., Liang, X. & Tian, Y. (2019) Geometric and kinematic features of a landslide in Mabian Sichuan, China, derived from UAV photography. *Landslides*, 16(2), 373–381. Available from: <https://doi.org/10.1007/s10346-018-1104-z>
- Mackey, B.H. & Roering, J.J. (2011) Sediment yield, spatial characteristics, and the long-term evolution of active earthflows determined from airborne LiDAR and historical aerial photographs, Eel River, California. *GSA Bulletin*, 123(7–8), 1560–1576. Available from: <https://doi.org/10.1130/B30306.1>
- Malet, J.-P., Laigle, D., Rémaitre, A. & Maquaire, O. (2005) Triggering conditions and mobility of debris flows associated to complex earthflows. *Geomorphology*, 66(1–4), 215–235. Available from: <https://doi.org/10.1016/j.geomorph.2004.09.014>
- Martínez-Carricondo, P., Agüera-Vega, F., Carvajal-Ramírez, F., Mesas-Carrascosa, F.J., García-Ferrer, A. & Pérez-Porras, F.J. (2018) Assessment of UAV-photogrammetric mapping accuracy based on variation of ground control points. *International Journal of Applied Earth Observation and Geoinformation*, 72, 1–10. Available from: <https://doi.org/10.1016/j.jag.2018.05.015>

- McKean, J. & Roering, J. (2004) Objective landslide detection and surface morphology mapping using high-resolution airborne laser altimetry. *Geomorphology*, 57(3-4), 331–351. Available from: [https://doi.org/10.1016/S0169-555X\(03\)00164-8](https://doi.org/10.1016/S0169-555X(03)00164-8)
- Meisina, C. (2004) Swelling-shrinking properties of weathered clayey soils associated with shallow landslides. *Quarterly Journal of Engineering Geology and Hydrogeology*, 37(2), 77–94. Available from: <https://doi.org/10.1144/1470-9236/03-044>
- Monjuvent, G. (1973) La transfluence Durance-Isère. Essai de synthèse du Quaternaire du bassin du Drac (Alpes françaises). *Géologie Alpine*, 49, 57–118.
- Moulin, C. & Robert, Y. (2004) Le glissement de l'Harmalière sur la commune de Sinard. p 11.
- Nappo, N., Mavrouli, O., Nex, F., van Westen, C., Gambillara, R. & Michetti, A.M. (2021) Use of UAV-based photogrammetry products for semi-automatic detection and classification of asphalt road damage in landslide-affected areas. *Engineering Geology*, 294, 106363. Available from: <https://doi.org/10.1016/j.enggeo.2021.106363>
- Niethammer, U., James, M.R., Rothmund, S., Travelletti, J. & Joswig, M. (2012) UAV-based remote sensing of the super-Sauze landslide: Evaluation and results. *Engineering Geology*, 128, 2–11. Available from: <https://doi.org/10.1016/j.enggeo.2011.03.012>
- Pardini, G., Guidi, G.V., Pini, R., Regiùs, D. & Gallart, F. (1996) Structure and porosity of smectitic mudrocks as affected by experimental wetting–Drying cycles and freezing–Thawing cycles. *Catena*, 27(3-4), 149–165. Available from: [https://doi.org/10.1016/0341-8162\(96\)00024-0](https://doi.org/10.1016/0341-8162(96)00024-0)
- Pawluszek, K., Borkowski, A. & Tarolli, P. (2018) Sensitivity analysis of automatic landslide mapping: Numerical experiments towards the best solution. *Landslides*, 15(9), 1851–1865. Available from: <https://doi.org/10.1007/s10346-018-0986-0>
- Peternel, T., Kumelj, Š., Oštir, K. & Komac, M. (2017) Monitoring the Potoška Planina landslide (NW Slovenia) using UAV photogrammetry and tachymetric measurements. *Landslides*, 14(1), 395–406. Available from: <https://doi.org/10.1007/s10346-016-0759-6>
- Picarelli, L., Urciuoli, G., Ramondini, M. & Comegna, L. (2005) Main features of mudslides in tectonised highly fissured clay shales. *Landslides*, 2(1), 15–30. Available from: <https://doi.org/10.1007/s10346-004-0040-2>
- Pineda, J.A., Alonso, E.E. & Romero, E. (2014) Environmental degradation of claystones. *Géotechnique*, 64(1), 64–82. Available from: <https://doi.org/10.1680/geot.13.P.056>
- Puniach, E., Gruszczynski, W., Cwiakata, P. & Matwij, W. (2021) Application of UAV-based orthomosaics for determination of horizontal displacement caused by underground mining. *ISPRS Journal of Photogrammetry and Remote Sensing*, 174, 282–303. Available from: <https://doi.org/10.1016/j.isprsjprs.2021.02.006>
- QGIS DT. (2020) QGIS Geographic Information System.
- Regiùs, D., Pardini, G. & Gallart, F. (1995) Regolith behaviour and physical weathering of clayey mudrock as dependent on seasonal weather conditions in a badland area at Vallcebre, eastern Pyrenees. *Catena*, 25(1-4), 199–212. Available from: [https://doi.org/10.1016/0341-8162\(95\)00010-P](https://doi.org/10.1016/0341-8162(95)00010-P)
- Remondino, F., Spera, M.G., Nocerino, E., Menna, F. & Nex, F. (2014) State of the art in high density image matching. *The Photogrammetric Record*, 29(146), 144–166. Available from: <https://doi.org/10.1111/phor.12063>
- Renalier, F., Bièvre, G., Jongmans, D., Campillo, M. & Bard, P.Y. (2010) Characterization and Monitoring of Unstable Clay Slopes Using Active and Passive Shear Wave Velocity Measurements. Advances in near-surface seismology and ground-penetrating radar Society of Exploration Geophysics, Tulsa 397–414. <https://doi.org/10.1190/1.9781560802259.ch24>
- Riley, S.J., DeGloria, S.D. & Elliot, R. (1999) A terrain ruggedness index that quantifies topographic heterogeneity. *Intermountain Journal of Sciences*, 5, 23–27.
- Rossi, G., Tanteri, L., Tofani, V., Vannocci, P., Moretti, S. & Casagli, N. (2018) Multitemporal UAV surveys for landslide mapping and characterization. *Landslides*, 15(5), 1045–1052. Available from: <https://doi.org/10.1007/s10346-018-0978-0>
- Samodra, G., Ramadhan, M.F., Sartohadi, J., Setiawan, M.A., Christanto, N. & Sukmawijaya, A. (2020) Characterization of displacement and internal structure of landslides from multitemporal UAV and ERT imaging. *Landslides*, 17(10), 2455–2468. Available from: <https://doi.org/10.1007/s10346-020-01428-0>
- Scheffler, D., Hollstein, A., Diedrich, H., Segl, K. & Hostert, P. (2017) AROSICS: An automated and robust open-source image co-registration software for multi-sensor satellite data. *Remote Sensing*, 9(7), 676. Available from: <https://doi.org/10.3390/rs9070676>
- Shepard, M.K., Campbell, B.A., Bulmer, M.H., Farr, T.G., Gaddis, L.R. & Plaut, J. J. (2001) The roughness of natural terrain: A planetary and remote sensing perspective. *Journal of Geophysical Research: Planets*, 106(E12), 32777–32795. Available from: <https://doi.org/10.1029/2000JE001429>
- Snavely, N., Seitz, S.M. & Szeliski, R. (2008) Modeling the world from internet photo collections. *International Journal of Computer Vision*, 80(2), 189–210. Available from: <https://doi.org/10.1007/s11263-007-0107-3>
- Stumpf, A., Malet, J.-P., Allemand, P. & Ulrich, P. (2014) Surface reconstruction and landslide displacement measurements with Pléiades satellite images. *ISPRS Journal of Photogrammetry and Remote Sensing*, 95, 1–12. Available from: <https://doi.org/10.1016/j.isprsjprs.2014.05.008>
- Tehrani, F.S., Santinelli, G. & Herrera Herrera, M. (2021) Multi-regional landslide detection using combined unsupervised and supervised machine learning. *Geomatics, Natural Hazards and Risk*, 12(1), 1015–1038. Available from: <https://doi.org/10.1080/19475705.2021.1912196>
- Travelletti, J., Malet, J.-P., Samyn, K., Grandjean, G. & Jaboyedoff, M. (2013) Control of landslide retrogression by discontinuities: Evidence by the integration of airborne- and ground-based geophysical information. *Landslides*, 10(1), 37–54. Available from: <https://doi.org/10.1007/s10346-011-0310-8>
- Turner, D., Lucieer, A. & Watson, C. (2012) An automated technique for generating Georectified mosaics from ultra-high resolution unmanned aerial vehicle (UAV) imagery, based on structure from motion (SfM) point clouds. *Remote Sensing*, 4(5), 1392–1410. Available from: <https://doi.org/10.3390/rs4051392>
- Uhlemann, S., Hagedorn, S., Dashwood, B., Maurer, H., Gunn, D., Dijkstra, T. & Chambers, J. (2016) Landslide characterization using P- and S-wave seismic refraction tomography – The importance of elastic moduli. *Journal of Applied Geophysics*, 134, 64–76. Available from: <https://doi.org/10.1016/j.jappgeo.2016.08.014>
- Walstra, J., Chandler, J.H., Dixon, N. & Dijkstra, T.A. (2007) Aerial photography and digital photogrammetry for landslide monitoring. *Geological Society, London, Special Publications*, 283(1), 53–63. Available from: <https://doi.org/10.1144/SP283.5>
- Wasowski, J. & Bovenga, F. (2022) Chapter 11 - Remote sensing of landslide motion with emphasis on satellite multi-temporal interferometry applications: an overview. In: Davies, T., Rosser, N. & Shroder, J. F. (Eds.) *Landslide Hazards, Risks, and Disasters*, Second edition. Elsevier, pp. 365–438.
- Westoby, M.J., Brasington, J., Glasser, N.F., Hambrey, M.J. & Reynolds, J.M. (2012) 'Structure-from-motion' photogrammetry: A low-cost, effective tool for geoscience applications. *Geomorphology*, 179, 300–314. Available from: <https://doi.org/10.1016/j.geomorph.2012.08.021>
- White, A.F. (2003) 5.05 - Natural Weathering Rates of Silicate Minerals. In: Holland, H.D. & Turekian, K.K. (Eds.) *Treatise on geochemistry*. Oxford: Pergamon, pp. 133–168.
- Zou, W., Ding, L., Han, Z. & Wang, X. (2020) Effects of freeze-thaw cycles on the moisture sensitivity of a compacted clay. *Engineering Geology*, 278, 105832. Available from: <https://doi.org/10.1016/j.enggeo.2020.105832>

How to cite this article: Fiolleau, S., Jongmans, D., Bièvre, G., Chambon, G., Michel, O. & Borgniet, L. (2022) Study of clay degradation in an earthslide combining OBIA and roughness analysis of UAV-based optical images. *Earth Surface Processes and Landforms*, 47(15), 3465–3480. Available from: <https://doi.org/10.1002/esp.5468>

APPENDIX 1

OBIA classifications of 24 May 2018; 18 July 2018 and 24 June 2019 acquisitions (RGB images with selected samples [ground truth], Classification, Accuracy between 0 and 100%)



APPENDIX 2

OBIA parametrization

The OBIA classification method is composed of two steps: The segmentation and the classification.

The objective of the segmentation is to define each intact clay block with a minimum number of segments. To do this, a trial-and-error exploration was carried out. Using the multi-resolution segmentation of the eCognition software, three parameters must be configured. The scale parameter (SP) defines the degree of heterogeneity allowed (the higher the SP, the higher the heterogeneity of the object). The shape parameter defines the influence ratio between the shape and the colour. The higher the value the lower the influence of the colour (between zero and one). The compactness parameter corresponds to the product of the width and the length over pixels numbers limit. The higher the value, the more compact the object (between zero and one).

The shape parameter is configured to give more weight to the shape than to the colour of the object since the colours are close between the different classes. The compactness is set to an average value in order to give the algorithm freedom of exploration. In the end, the parameter having the most impact is the SP. This one has been set to 50, allowing sufficient heterogeneity within the object to obtain a satisfactory result (e.g. Figure A1).

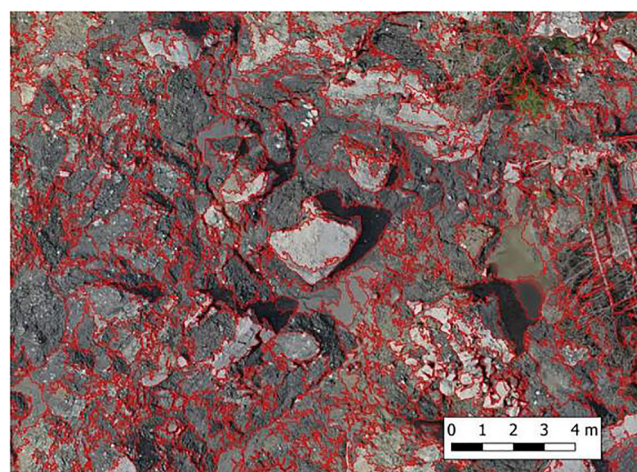


FIGURE A1 Zoom on segmentation of 24 May 2018 orthophoto: [Color figure can be viewed at wileyonlinelibrary.com]

TABLE A1 Decision tree parameters

Features	Mean (layers 1, 2, 3 and 4), standard deviation (layers 1, 2, 3 and 4)
Type	Decision tree
Maximum categories	16
Cross-validation folds	3
Truncate pruned tree	Yes

The decision tree classifier of the eCognition software was then chosen to perform the supervised classification step.

The principle is to classify a set of data by subjecting it to a series of decisions based on the feature's values. Here, the mean and standard deviation of each layer (RGB and roughness) were chosen. The training dataset is partitioned according to a feature value, and recursively partitioning each subset until the dataset is all members of the same class or until recursion adds no value to the classification. A trial-and-error approach was used to adjust the different parameters to converge towards the best classification (Table A1).

The maximum categories number, specifying the maximum number of categories into which data can be grouped at a given level, has been set to 16. A reasonable number to reduce processing time while preserving accuracy. The cross-validation folds were set to three, allowing the model to be compared to the training data to assess accuracy. The truncate prune tree parameter enabled to remove unnecessary branches.